scientific reports

Check for updates

OPEN

Experimental investigation of blasting stress wave attenuation in sandstone with columnar charging using high-speed DIC technique

Li Chengjie[1,2,3,4]✉, Wang Mengqi[1,3], Xie Shoudong[1,3,4], An Qi[1,2,3] & Yu Mengyao[1,3]

The propagation and attenuation characteristics of blast stress waves in geotechnical media directly influence the fracture behavior of the medium and serve as a crucial basis for optimizing blasting parameter design. To examine the attenuation characteristics of cylindrical blast waves in rocks, the indoor blasting experiments were conducted using sandstone with cylindrical charges. Digital image correlation technology was employed to successfully capture the full-field strain evolution around the borehole during blasting, and the strain–time curves of the rock surrounding the borehole were obtained. To account for the influence of blasting stress wave loading rates on dynamic elastic modulus, Split Hopkinson Pressure Bar tests were performed to establish a precise relationship between dynamic elastic modulus and strain rate. By analyzing the attenuation of the peak strain, a stress wave attenuation equation within the fractured zone was developed, and the stress wave attenuation index was examined. The results indicated that the experimental method effectively simulated the blasting process of cylindrical charges. The strain wave propagation was accompanied by energy transformation, where the descending phase of the strain–time curve represented the rapid energy input to the rock near the borehole due to blast loading, whereas the ascending phase reflected the radial release of elastic energy, further promoting the development of circumferential cracks, albeit at a lower energy release rate than the descending phase. As the distance from the blast center increased, both the dynamic elastic modulus and strain rate of the rock under blast loading decreased, leading to differences between the attenuation characteristics of stress waves and strain waves, with the former following a power function decay. The complex nature of stress wave attenuation in rocks was primarily governed by physical attenuation properties, with the physical attenuation index exceeding the geometric attenuation index in crushed and cracked zones. Finally, the accuracy of the stress wave attenuation equation and the reliability of the experimental method were validated by analyzing the fracture morphology of the blasted specimens and the extent of the cracked zone.

Keywords Blasting cylindrical wave, DIC, Strain field evolution, Dynamic elastic modulus, Stress wave attenuation, Blasting damage range

In geotechnical and mining engineering, the drilling and blasting method remains one of the most widely used and efficient techniques for excavating hard rock masses[1,2]. Determining the damage zone around a borehole is a critical factor in the design and optimization of blasting network parameters. The stress waves generated by columnar charge blasting can be conceptualized as waves radiating from a line source in a plane perpendicular to the axis and propagating outward as circular wavefronts within the surrounding medium[3]. Therefore, accurately defining the damage zone resulting from a single-hole charge explosion requires an in-depth understanding of the propagation and attenuation characteristics of columnar stress waves. Upon detonation, an initial shock wave forms within the rock mass, which rapidly decays into a stress wave before transforming into seismic waves and eventually dissipating[4]. The attenuation of explosion-induced columnar waves generally follows either the power

[1]School of Civil Engineering and Architecture, Anhui University of Science and Technology, Huainan 232000, Anhui, China. [2]State Key Laboratory for Safe Mining of Deep Coal Resources and Environment Protection, Huainan 232000, Anhui, China. [3]Engineering Research Center of Underground Mine Construction, Ministry of Education, Anhui University of Science and Technology, Huainan 232000, Anhui, China. [4]Key Laboratory of Safety Intelligent Mining in Non-coal Open-pit Mines, National Mine Safety Administration, Guangzhou 510000, Guangdong, China. ✉email: austlcj@163.com

law or exponential decay functions as the distance from the explosion center increases[5–7], with both geometric and physical attenuation mechanisms contributing to this process. Geometric attenuation results from the radial expansion of the stress wave energy, causing a reduction in the energy density with increasing distance from the source[8]. Physical attenuation occurs owing to plastic deformation in the rock material, which dissipates part of the wave energy and leads to further stress wave attenuation[9]. As stress waves propagate, they create distinct damage zones at varying distances from the borehole, including crushed, cracked, and elastic vibration zones[10], each with different energy consumption levels that influence the stress wave attenuation rates. Consequently, the propagation and attenuation behavior of explosion-induced columnar waves in rock masses is significantly more complex than that of elastic columnar waves.

Since the 1970s, researchers have extensively employed theoretical models[11,12], experimental investigations[13,14], and numerical simulations[15] to investigate blasting damage effects and stress wave attenuation in rock masses. Rock blasting, particularly with columnar charge configurations, is a highly complex dynamic fracture process in which the dynamic mechanical properties of the rock and stress wave propagation are difficult to quantify accurately[16]. Consequently, theoretical and numerical analyses of stress wave attenuation often rely on assumptions about rock dynamic behavior and attenuation mechanisms under specific conditions or on experimental data that are not always verifiable through direct field validation. With advancements in pressure and deformation measurement techniques, physical modeling experiments have become an effective approach for capturing the stress-wave attenuation process under controlled conditions[17,18]. For instance, Huo et al.[19] implemented mortar-based blasting models to examine the effects of filling media and decoupling coefficients on stress wave propagation, whereas Qiu et al.[20] investigated the deformation disturbances caused by charge blasting in underground tunnels using similar models. These rock-like materials enable the direct acquisition of stress wave data at specific locations through embedded pressure or strain sensors. However, capturing the internal deformation of natural rock and fabricated rock-like materials remains challenging, necessitating the placement of deformation measurement devices on the surface of the medium[21]. Alternatively, non-contact full-field stress and strain measurement techniques such as dynamic photoelasticity[22], dynamic caustics[23], and DIC[24] provide indirect methods for observing wave propagation and deformation characteristics. For example, Malezhik et al.[25] applied the dynamic photoelasticity to analyze the stress fields around tunnels in anisotropic media under impact loading, while Yang et al.[26,27] conducted the explosive tests on PMMA, a rock-like material, using dynamic caustics to observe the crack propagation and strain distribution. Additionally, He et al.[28] monitored the deformation process of rock surrounding boreholes under confining pressure through using high-speed imaging combined with DIC techniques. Despite these advancements, challenges persist owing to the scale limitations of laboratory models, rapid nature of explosive detonations, and inherent randomness and complexity of rock fragmentation near boreholes. These factors contribute to incomplete observation coverage and deviations from idealized conditions for columnar wave propagation, complicating the precise measurement of rock deformation in the vicinity of columnar charge blasts.

In summary, to accurately capture the propagation characteristics of columnar blasting stress waves, rock blasting strain wave propagation experiments under columnar charge conditions should not only constrain the side surfaces of the model but also limit the displacement along the borehole direction. Traditional experimental methods that arrange the measurement elements within or on the surface of the model can only capture the deformation at a limited number of points. Therefore, incorporating full-field surface testing techniques is beneficial for obtaining a larger volume of test data. In this study, we enhanced the specimen constraint setup and integrated high-speed photography with DIC techniques as a widely used method for surface deformation observation in geotechnical materials. These methods were applied to model experiments on strain fields during columnar charge rock blasting, enabling a detailed investigation of the stress wave propagation and attenuation processes and an analysis of the stress wave attenuation exponent.

Overview of blasting test scheme

Specimen preparation

For this experiment, a relatively homogeneous sandstone with the density of 2710 kg m^{-3} and the Poisson's ratio of 0.20 was selected. To facilitate full-field specimen visualization and experimental operations, specimens measuring 300 mm × 300 mm × 50 mm were prepared. After smoothing its surface, matte white paint was applied to the observation side as a background, followed by black speckle dots with a marker. The size and density of the dots were optimized based on the best processing results obtained using DIC software (Fig. 1). A vertical borehole was drilled at the geometric center on the back of the specimen, with a diameter slightly larger than that of the detonator (approximately 8 mm) and a depth of 45 mm. A 5 mm section was left undrilled to prevent premature detonation and exposure of the blast products, which could interfere with imaging. A 1 g electric detonator served as the explosive source to simulate the columnar charge environment, with passive confinement achieved using the device shown in Fig. 1. The foam material was placed between the sides of the specimen and the cushion blocks to minimize the stress wave reflection and extension effects. The specimen was confined to both the front and rear using high-strength transparent resin plates, ensuring radial propagation of the explosive force along the borehole axis while enhancing the safety and improving the imaging conditions. Moreover, a thin transparent rubber pad was inserted between the resin plates and specimen to protect the surface speckle pattern from damage. This configuration effectively simulates cylindrical charge conditions by directing detonation energy predominantly along the borehole radial direction.

Strain field acquisition

Using the arrangement of speckle patterns and pre-blast images as references, the entire specimen area was selected as the reference sub-region, with its center positioned at the geometric center of the specimen, corresponding to the borehole center. The images captured before and after the blast were divided into

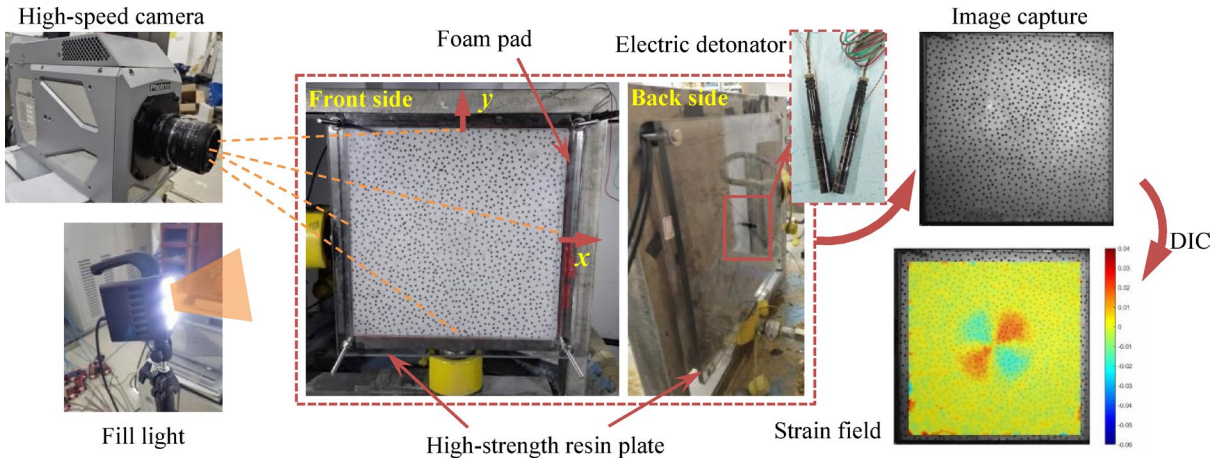

Fig. 1. Specimen confinement preparation and charge blasting process.

grids, and the sub-regions were analyzed using specific correlation functions[29,30]. Following blasting, the surface deformation causes displacement of the speckle patterns. By analyzing the correlation coefficients of grayscale values representing these changes, the spatial positions and displacements of the points before and after deformation were determined. This enabled the acquisition of strain field evolution around the borehole throughout the blasting process. The key requirement for obtaining complete strain field evolution using DIC techniques was to capture a sufficient number of high-quality images. A high-speed camera with a maximum frame rate of 2×10^5 fps was used in this experiment. During testing, the camera was positioned vertically, and the image capture frequency was set to 10^5 fps, ensuring full-field imaging of the specimen. Experimental results confirmed that this frame rate yielded sufficiently clear images of the blasting process, thereby enabling accurate reconstruction of the strain field evolution.

Evolution of the specimen strain field during the blasting process

Strain contour characteristics of the specimen

A series of images captured during the blasting process were processed, and within the 300×300 mm internal area of the specimen, 384×384 virtual points were assigned, with the distance between adjacent points corresponding to an actual length of approximately 0.78 mm. Figure 2 illustrates the strain contour maps in the *x*-direction (horizontal), *y*-direction (vertical), and *xy*-direction ($\pm 45°$ and $\pm 135°$) during blasting with a time interval of 50 μs between adjacent images. The results indicated that the radial strain in all three directions followed an approximately symmetrical distribution centered around the borehole. Additionally, the strain magnitudes in different directions were nearly equal and negative, demonstrating that the deformation propagated radially outward from the borehole in the form of compressive strain at a uniform speed. This confirmed that the blasting strain wave propagated in an approximately cylindrical waveform, validating the suitability of the experimental method for columnar charge blasting tests. At the center of the specimen, the deformation was more pronounced and manifested as tensile strain owing to the focusing effect of the detonator explosion, which caused a small central rock mass to exhibit outward projectile motion. However, the presence of the front and rear resin plates restricted the development of tensile deformation in this region.

Strain field evolution characteristics

Specimen deformation area division

To capture the radial propagation of the strain wave along the borehole, the strain–time curves at different distances from the explosion center were analyzed. Because the blasting strain wave propagated outward in a cylindrical waveform, the strain data from various positions along the OC segment on the x-axis in the middle of the specimen (Fig. 3a) were selected for analysis. The radial strain–time variations at the virtual points along the OC segment are shown in Fig. 3b and c. The characteristic changes in these curves indicated that the rock near point O experienced tensile deformation owing to the focusing effect of detonator charge, as previously discussed. Moving from O to A, the rock transitioned from a tensile to a compressive state, with point A corresponding to the location of the maximum peak compressive strain. Furthermore, data processing revealed that despite the application of foam pads to mitigate boundary effects, significant reflection tensile waves were still present. As the primary focus of this study was the strain wave behavior before and at the peak value, the AB segment, characterized by an undisturbed pre-peak waveform, was selected for strain wave analysis, where the time-history curve at point B quantitatively demonstrates the compressive strain peak characteristics. Based on points A and B, the OC segment of the specimen was divided into three regions: OA, AB, and BC, measuring approximately 35, 70, and 45 mm, respectively. These corresponded to three annular rock deformation zones around the borehole during blasting, designated as Ω_1, Ω_2, and Ω_3. Notably, points A and B coincided with the virtual measurement points. Although the corresponding Ω_1, Ω_2, and Ω_3 regions exhibited slight variations in area among different specimens, these dimensional differences did not affect the experimental results analysis.

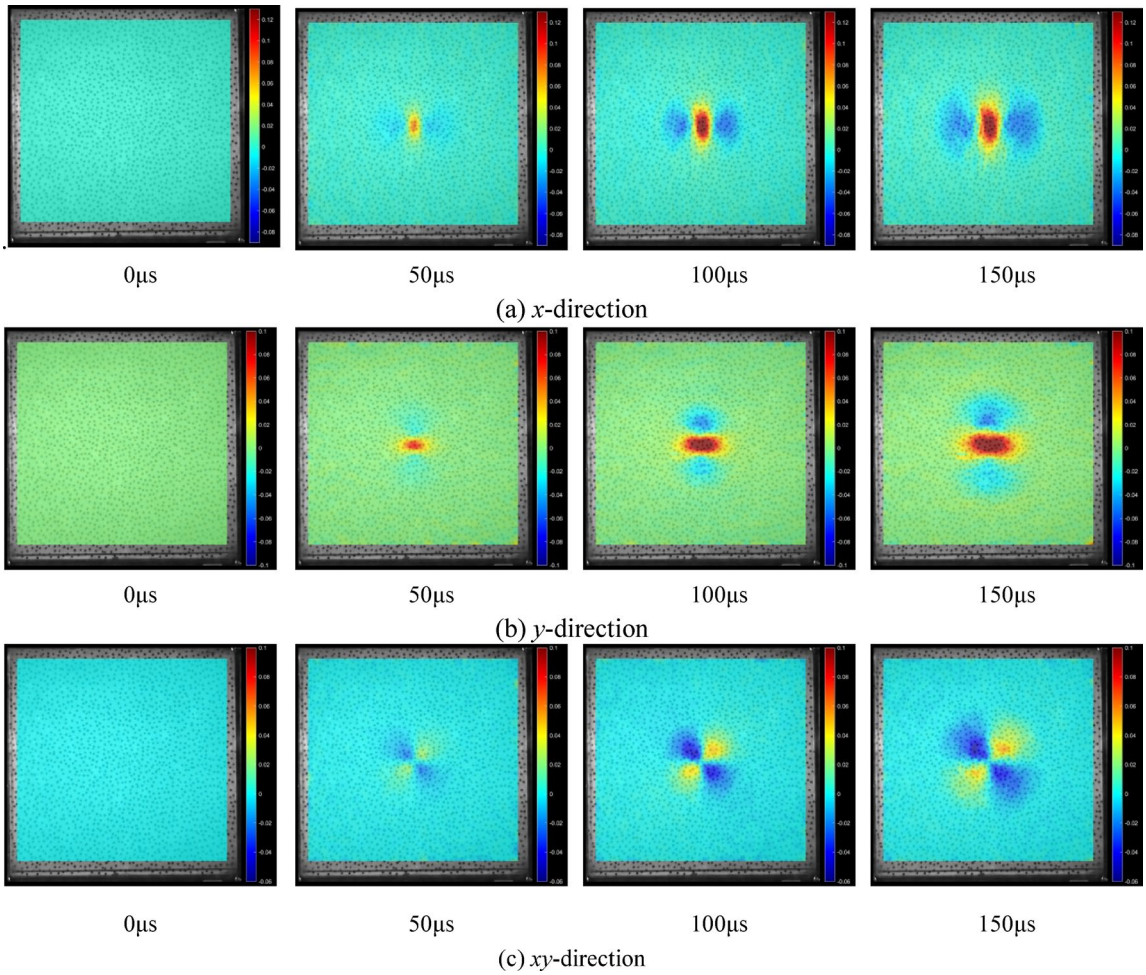

Fig. 2. Evolution of specimen strain field during the blasting process.

In the Ω_1 region, the rock fragments exhibited an outward motion trend. Near point O, the strain was tensile, initially increasing rapidly in an approximately linear manner, before gradually decreasing and stabilizing. As the position shifted from point O to the Ω_1 region boundary, the initial deformation transitioned from tensile to compressive, with a characteristic pattern of first compression followed by tension. Closer to the Ω_1 region boundary, the compressive strain peak increased, duration of the compressive strain increased, and duration of the tensile strain decreased. Near the boundary, the medium underwent almost exclusive compressive deformation. In the Ω_2 region, the specimen was subjected only to compressive stress (Fig. 3c). Near point A in the Ω_1 region, a transition from compressive to tensile strain occurred, indicating that the rock medium at this position experienced compression followed by tension during the blasting process. This phenomenon can be explained as follows.

As shown in Fig. 4, immediately after the explosion, a shock wave formed along the borehole wall, causing intense damage to the surrounding rock. High-temperature, high-pressure blast gases can further exacerbate this damage, creating an enlarged cavity and a network of crushed zones where the rock primarily undergoes compressive-shear failure[31]. This process rapidly transitions from a shock wave to a stress wave. Although incapable of inducing compressive-shear failure, these stress waves continue radial compression on rock, generating tangential tensile stresses through Poisson's effect. This leads to tangential deformation and forms a cracked zone dominated by radial cracks. The quasi-static gas wedge effect of blast gases accelerates the expansion of this cracked zone, where the rock predominantly experiences tensile failure[32]. As the stress wave further attenuates into seismic waves, it ceases to cause significant damage, leading to the formation of an elastic vibration zone. The high-intensity and short duration of the blast shock wave generated rapid compressive deformation in the adjacent rock mass, accumulating substantial elastic strain energy. When the shock wave decays to a point where it can no longer transfer energy to compressed rock, the accumulated elastic strain energy propagates radially outward as a stress wave. Simultaneously, this energy can be released radially inward into the crushed zone and expanded cavity, generating a circumferential unloading wave that further accelerates the development of circumferential cracks. Therefore, under columnar charge conditions, the rock medium in the near-borehole region initially experienced compressive stress in the early stages of blasting, followed by tensile stress in the later stages.

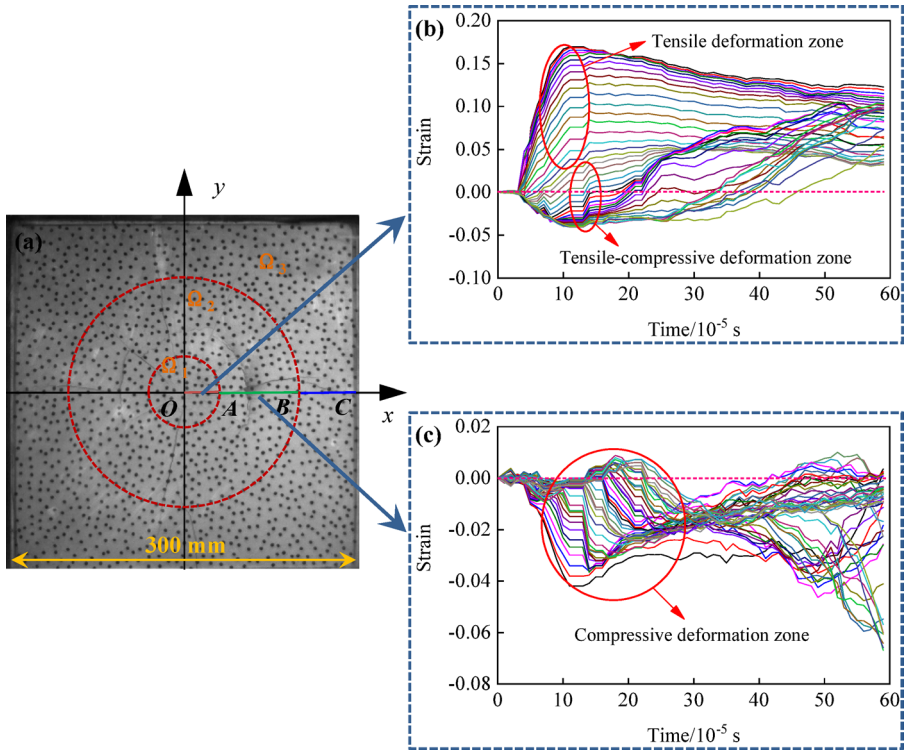

Fig. 3. Division of strain time history curves for different zones: (**a**) division of deformation zones around the borehole, (**b**) strain time history variation at OA segment measuring points, and (**c**) strain time history variation at AB segment measuring points.

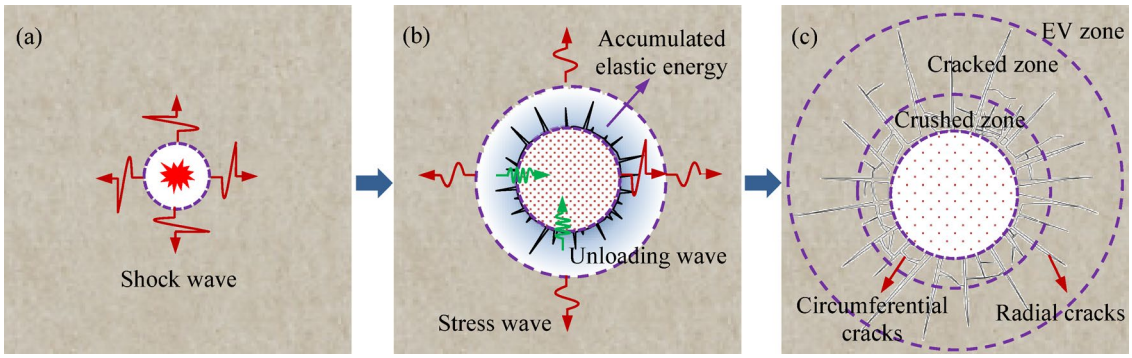

Fig. 4. Schematic diagram of rock mass deformation and damage around the blasthole under blasting load: (**a**) explosion onset, (**b**) shock wave impact, and (**c**) damage zone formation. EV zone: elastic vibration zone.

From the above analysis, the deformation of the medium in the small Ω_1 region was not caused by the cylindrical wave effect owing to the energy-focusing cavity of the detonator, despite the implementation of the front and rear confinement plates in this experiment. In addition, in the Ω_3 region, the strain wave before reaching its peak was influenced by the reflected tensile wave. In contrast, the Ω_2 region was directly affected by the cylindrical stress wave and was primarily associated with rock fractures. Therefore, this study focused on analyzing the attenuation characteristics of strain waves in the Ω_2 region.

Radial strain–time curve characteristics

Because of the large volume of data, one research point was selected for every 10 virtual points along the AB segment, obtaining a spacing of 7.8 mm between adjacent research points and a total of 10 measurement points, starting from point A. The curves in Fig. 3c underwent appropriate smoothing treatment without altering their evolutionary trends, peak magnitudes, descending edge slopes, or peak values, as shown in Fig. 5, where the numbers represent the distances of the measurement points from point A. In the Ω_2 region, the compressive strain increased rapidly over time, reached a peak, and then gradually decreased. Overall, the peak compressive strain decreased over time. The rate of decrease along the descending slope of the curve decreased, and the

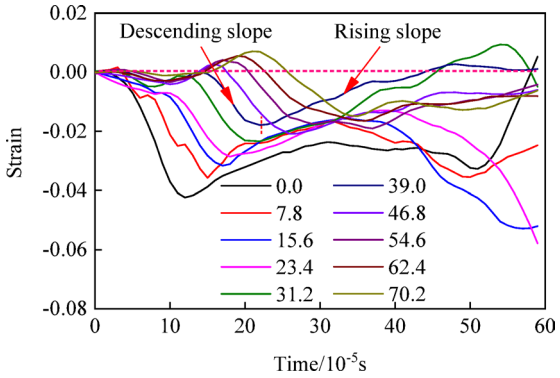

Fig. 5. Radial strain time history curves of selected points in the Ω_2 region.

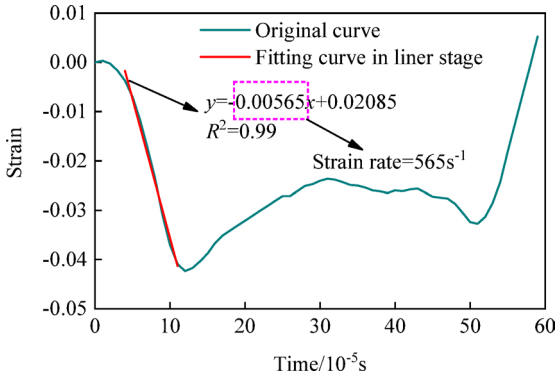

Fig. 6. Strain rate fitting for the compression phase of rock medium.

duration of this phase was shorter than that of the rising slope. In reality, the descending slope represents the stress wave rapidly compressing the specimen, whereas subsequent deformation recovery occurs once the rock medium has accumulated sufficient energy. The longer duration of the recovery process compared to the compression phase can be attributed to the rapid outward propagation of the initial blasting stress wave from the borehole center, whereas in the later stage, the release of accumulated elastic energy can induce an inward radial motion of the rock medium. This inward motion encounters greater resistance and, because the stored elastic energy is inevitably lower than the energy carried by the compressive stress wave, the release rate decreases, leading to an extended duration of the rising slope. The inflection point between descending and ascending phases marks the transition from compression to tensile deformation. Maximum radial compressive stress at any position coincides with peak deformation rate. Subsequent stress reduction triggers compressive deformation recovery, precisely defining the compressive-tensile deformation transition point.

Figure 5 illustrates that the strain–time curve demonstrates an initial compressive deformation of the rock surrounding the borehole under the blasting load, followed by partial deformation recovery, whereas it cannot return to the baseline position. This suggests that the process led to significant irreversible deformation, indicating that the medium sustained damage or yielded. Given that rock was a brittle material, this yielding or damage was primarily concentrated in the compressive deformation phase, which occurred before the peak strain. The variation in the strain rate during compression reflected the characteristics of the rock medium to the blasting dynamic load. As shown in Fig. 5, the strain–time curve at the measurement points generally exhibited a sinusoidal or approximately triangular shape, with the descending slope of the radial strain–time curve displaying a near-linear trend. This indicates that during the loading phase, the rock medium experienced a relatively constant strain rate change. By performing a linear fit on the descending slope, the slope value represented the strain rate at that location under the blasting load, as shown for point A in Fig. 6. The strain rates at each measurement point in the Ω_2 region are shown in Fig. 7, revealing a general decrease in the strain rate with increasing distance from the explosion center. Beyond approximately 7 cm, the strain rate declined from approximately 565 s^{-1} to approximately 196 s^{-1}.

Characteristics of blasting stress wave attenuation

In engineering practice, determining the stress wave attenuation law is essential in addition to understanding the strain wave attenuation process. In the near field of the explosion, the stress wave attenuates rapidly, leading to significant variations in the strain rate, while the rock at different distances from the borehole exists in varying elastic–plastic states. Rock-like materials can exhibit a pronounced strain rate effect under loading, with their

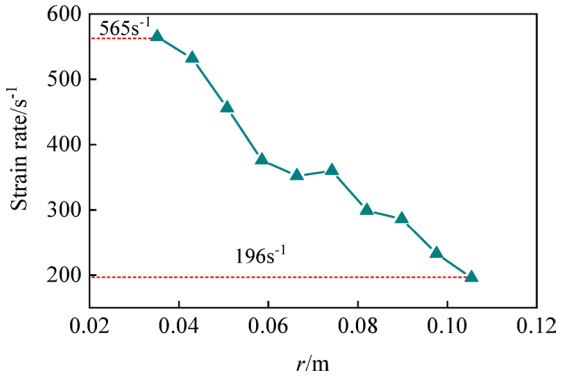

Fig. 7. Correlation between strain rate and distance from blast center.

elastic modulus dependent on the strain rate[33,34]. Consequently, the relationship between the radial stress and radial strain varies with distance from the explosion center. As previously discussed, the relationship between the strain rate and the distance from the explosion center was established. In the following section, based on the correlation between the elastic modulus and strain rate, the relationship between the elastic modulus and distance from the explosion center was determined. This can facilitate the derivation of the radial stress peak attenuation law as a function of the distance from the explosion center using the stress–strain relationship.

Relationship between elastic modulus and strain rate

In the Ω_2 region, the strain rates induced by the blasting stress wave range from 196 to 565 s^{-1}, falling within the moderate strain rate range of the study[35]. The Split Hopkinson Pressure Bar (SHPB) system, which is a widely used apparatus for testing the dynamic properties of rock-like materials at moderate strain rates, can generate stress waveforms similar to blasting stress waves when using tapered striker bars[36]. Therefore, SHPB impact loading tests were conducted on the sandstone specimens at four different impact velocities corresponding to four distinct strain rates, with each velocity tested on more than three valid specimens. Figure 8 shows the dynamic stress–strain curves for the selected sandstone specimens at these strain rates. Consistent with the strain rate values in Fig. 6 under blasting loading, the average strain rate of the approximately linear deformation segment of the specimen was considered as the loading strain rate. Because this study primarily focused on the variation in peak stress or strain wave values, the secant modulus at the peak point of the dynamic stress–strain curve was used as the dynamic elastic modulus of the specimen.

As the loading rate of rock-like materials increases, their elastic moduli generally increase. Studies have shown that within a certain strain rate range, the dynamic elastic modulus of rock-like materials exhibits either an approximately linear[37] or logarithmic[38,39] increase. Based on the experimental results, the dynamic elastic modulus of sandstone in the Ω_2 region follows a logarithmic function with the strain rate. From the SHPB test results, as the strain rate increased from 85.96 to 151.83 s^{-1}, the dynamic elastic modulus of the specimen rose from 9.67 to 17.24 GPa. This relationship was fitted to establish a predictive model for the dynamic elastic modulus as a function of strain rate (Fig. 9). By integrating this relationship with the strain rate $\dot{\varepsilon}$ and distance from the explosion center (r) in Fig. 7, the correlation between dynamic elastic modulus $E(r)$ and explosion center distance (r) was derived (Fig. 10). In the Ω_2 region, under the influence of the blasting stress wave, the dynamic elastic modulus of the rock gradually decreased from 35.72 to 20.69 GPa, demonstrating that the elastic modulus decreased as the distance from the explosion center increased.

Relationship between radial peak stress and explosion center distance

The relationship between radial stress and strain at a specific point in the rock medium surrounding the borehole can be expressed as follows:

$$\sigma_r = E(r)\,\varepsilon(r) \tag{1}$$

where σ_r and $\varepsilon(r)$ are the radial stress and strain, respectively, at a specific point within the rock medium.

By statistically analyzing the radial strain peak values at different measurement points from the strain–time curves, the variation in the radial strain peak values with respect to the explosion center distance (r) was obtained. Based on the dynamic elastic modulus and radial strain peak values, the relationship between the radial peak stress and explosion center distance was determined (Fig. 11). The results indicated that as the distance from the explosion center increased, the radial strain peak value in the Ω_2 region decreased from 0.043 to 0.015, whereas the radial peak stress decreased from 1522.17 to 318.63 MPa. Although both the strain and stress peak values decreased with increasing distance, their rates of decrease gradually slowed, with the stress peak values exhibiting a more pronounced reduction. This discrepancy resulted from the gradual decrease in the dynamic elastic modulus with increasing distance from the explosion center. If the dynamic elastic modulus remained constant, the trend of the stress peak values with respect to the explosion center distance would align with that of the strain peak values, resulting in a lower stress wave attenuation rate than that observed.

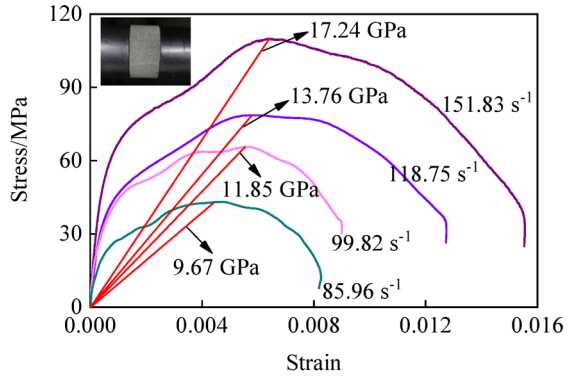

(a) Strain rate values of the specimen

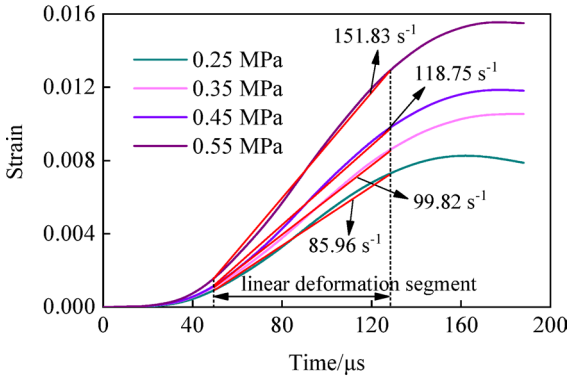

(b) Elastic modulus values of the specimen

Fig. 8. Determination of strain rate and elastic modulus of specimen based on SHPB test.

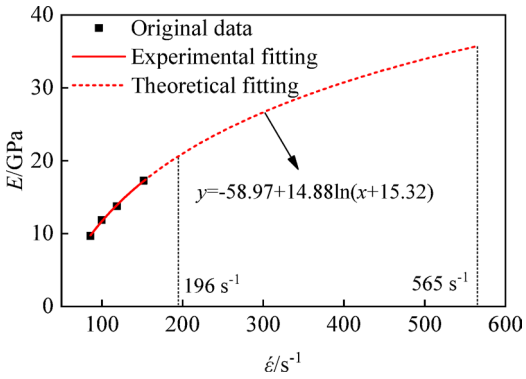

Fig. 9. Fitting of the variation in rock elastic modulus with strain rate.

Blasting stress wave attenuation equation

As shown in Fig. 11, the radial peak stress followed an approximately power-law relationship with the explosion center distance. Based on previous studies, the relationship between the shock wave and stress wave peak values and the explosion center distance within the rock medium can be expressed as follows[40,41]:

$$\sigma_{cru}^{r} = \sigma_i \left(r_0/r\right)^{\alpha} \tag{2}$$

$$\sigma_{cra}^{r} = \sigma_j \left(r_{cru}/r\right)^{\beta} \tag{3}$$

where σ_{cru}^{r} and σ_{cra}^{r} represent the radial compressive peak stresses in the crushed and cracked zones of the rock, respectively; σ_i is the initial radial compressive peak stress in the borehole wall rock; σ_j is the radial compressive peak stress at the interface between the crushed and cracked zones; r_0 and r_{cru} represent the borehole radius

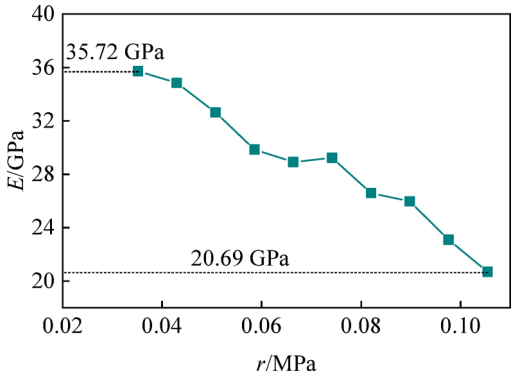

Fig. 10. Correlation between E and r.

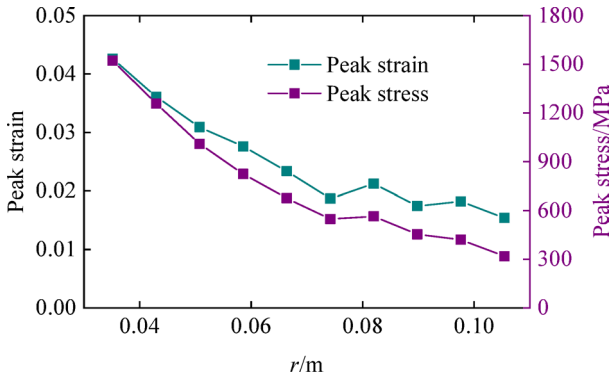

Fig. 11. Variation between radial peak strain and stress with respect to r.

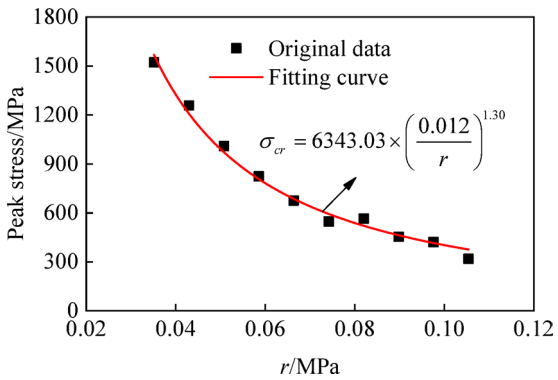

Fig. 12. Fitting curve of peak stress versus r.

and radius of the crushed zone, respectively (in m); and α and β represent the attenuation exponents of the shock wave and stress wave, respectively.

Research has shown that the radius of the crushed zone in rock blasting generally ranges from 2 to 5 r_0[42,43], whereas the radius of the cracked zone typically ranges between 10 and 40 r_0. The Ω_2 region lies within the range of 8 to 26 r_0 and can be considered as part of the cracked zone for simplicity. The relationship between the stress peak and explosion center distance in Fig. 11 was fitted using Eq. (3), where the r_{cru} values in Eq. (3) were initially fixed, and the parameters σ_j and β were subsequently determined. The results indicated that the crushed zone range did not significantly affect the fitting curve for the Ω_2 region. In this experiment, the borehole radius r_b was approximately 0.004 m, and a crushed zone radius of 3 r_0 was assumed (Fig. 12). The fitted curve aligns well with the original data, yielding an attenuation exponent of 1.30 and a radial stress of 6343.03 MPa at the interface between the crushed and cracked zones. In both Eqs. (2) and (3), the attenuation exponent was typically determined based on empirical data $\alpha = 2 + \mu_d/(1 - \mu_d)$ and $\beta = 2 - \mu_d/(1 - \mu_d)$,

where μ_d represents the dynamic Poisson's ratio of the rock. Assuming a Poisson's ratio of 0.16, the attenuation exponent was calculated to be 1.81. The slightly lower fitted result from this experiment may be attributed to the relatively lower defect density of the tested rock specimens, whereas the empirical attenuation exponent was derived from engineering rock masses with more inherent defects. Overall, the derived attenuation results were consistent with the general attenuation behavior of rock-like materials.

The overall stress-wave attenuation process depicted in the figure resulted from both geometric and physical attenuation. The geometric attenuation resembled the attenuation process of elastic waves originating from a cylindrical cavity, where the stress on the wavefront decayed at a velocity of $1/\sqrt{r}$[44–46]. Consequently, the complex characteristics of rock medium-blasting cylindrical wave attenuation are primarily governed by the physical attenuation properties of the stress wave, which are closely related to the rock's plastic loading behavior. By combining the geometric attenuation characteristics with the experimental attenuation results of the cylindrical stress wave in the rock, a physical attenuation equation was derived, which could be the attenuation equation for the one-dimensional blasting stress wave in the rock medium. The stress peak values in the geometric and physical attenuation processes are denoted as σ_g and σ_p, respectively, while the geometric attenuation of the cylindrical wave in the Ω_2 region follows the equation:

$$\sigma_g = \sigma_j \left(r_p/r\right)^{0.50} \tag{4}$$

By comparing Eqs. (3) and (4) and utilizing the fitting results in Fig. 12, the physical attenuation of the blasting stress wave can be expressed as

$$\sigma_p = \sigma_j \left(r_p/r\right)^{0.80} \tag{5}$$

Figure 13 illustrates the relationship between the attenuation rates of different types of decay and the explosion center distance, with the crushed zone radius set at 3 r_0. As the explosion center distance increased, the attenuation rates of all stress peak values gradually decreased, and in the Ω_2 region, the physical attenuation rate exceeded the geometric attenuation rate. The geometric attenuation coefficient of the shock wave remained the same in both the crushed and cracked zones. Conversely, owing to the more intense fragmentation of the rock in the crushed zone, physical attenuation occurred more rapidly. In addition, the relatively small size of the crushed zone suggested that the stress wave attenuation in this region was primarily governed by physical attenuation. Although the experiment did not determine the value of α, the stress attenuation coefficient in the crushed zone was significantly higher than that in the cracked zone, aligning with the shock wave and stress wave attenuation coefficient values proposed by other scholars[47–49].

Discussion on the accuracy of the stress wave attenuation law

In the previous section, the stress-wave attenuation equation fitting process assumed that the Ω_2 region lies within the cracked zone. The validity of this assumption and the accuracy of the resulting stress-wave attenuation law under this condition require further examination. Because the stress wave propagation and attenuation are influenced by the expansion of the geometric space and rock damage, the stress wave attenuation formula can be applied to calculate the rock damage range. By comparing the calculated damage range with the actual damage caused by the explosion, the accuracy of the stress wave attenuation law can be evaluated.

Characteristics of rock blasting failure patterns

The failure patterns of the specimens used in this experiment are shown in Fig. 14. Within a small region around the borehole (approximately 20 mm), the rock exhibited a distinct "bright white" color with friction marks, indicating the significant compressive-shear damage characteristic of the crushed zone. Four through-going cracks formed near the symmetrical axis of the borehole as stress waves propagating in two directions traveled the shortest distance and were the first to be affected by reflected tensile waves. The later portion of the compressive wave and the reflected tensile wave superimposed at the symmetrical axis, where the compressive

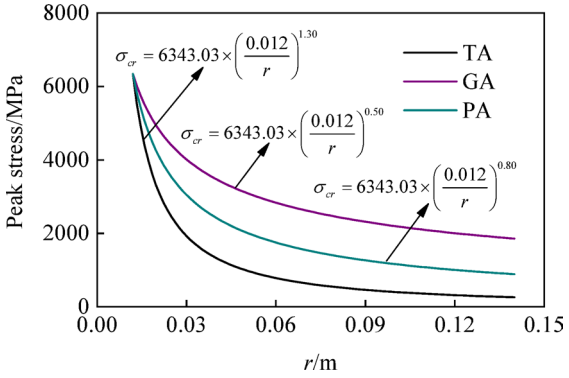

Fig. 13. Comparison of three types of attenuation curves: total attenuation, geometric attenuation, and physical attenuation.

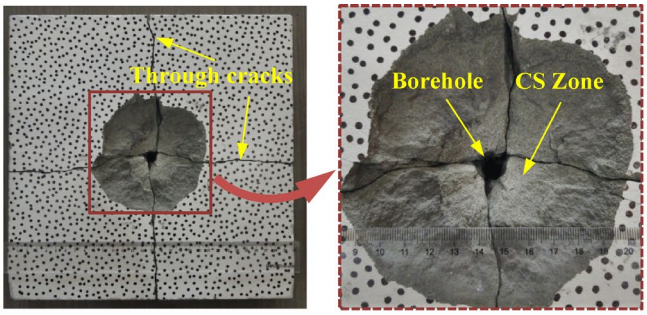

(a) Front view of the failure mode. CS Zone: compressive-shear zone

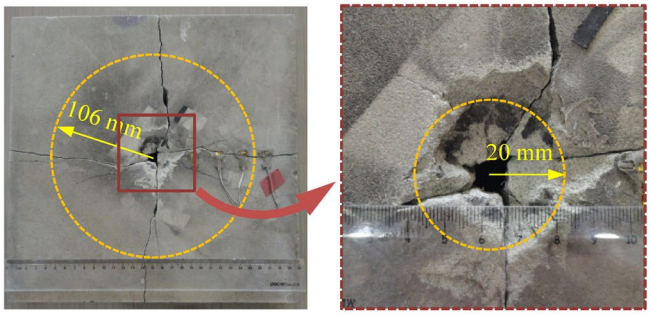

(b) Rear view of the failure mode

(c) Fracture surface morphological characteristics.

Fig. 14. Fracture morphology of specimen after blasting.

stress and vertically induced tensile stress reached their maximum, resulting in the "+"-shaped through cracks, as shown in Fig. 14. However, the lengths of these cracks did not represent the full extent of the cracked zone. To estimate its expansion, the lengths of several longer cracks were measured, with an approximate length of 106 mm. This suggested that the radius of the blasting crushed zone was within 5 r_0, whereas the radius of the cracked zone was at least 26 r_0. The Ω_2 region extended from 8 to 26 r_0, indicating that the stress attenuation results obtained above accurately reflected the stress wave attenuation law within the cracked zone. It should be noted that circumferential cracks described in previous sections are absent in this specimen,, whereas in practical engineering blasting operations, a significant network of cracks is indeed observed in the near-borehole region. This discrepancy originates from scale limitations in laboratory conditions, specifically specimen dimensions and charge quantities.

Calculation of blasting damage range

In the crushed zone, the rock primarily experienced compressive-shear failure, whereas in the cracked zone, it was mainly subjected to tangential tensile stress. By comparing the blasting stress waves with the dynamic compressive and tensile strengths of the rock in the respective regions, the radii of the crushed and cracked zones can be determined.

Crushed zone radius

A crushed zone was formed when the equivalent stress generated by the explosion stress wave in this area exceeded the dynamic compressive strength of the rock, as expressed by the following equation:

$$\sigma_i > \sigma_{dc} \tag{6}$$

σ_i can be expressed as[50]

$$\sigma_i = \frac{1}{\sqrt{2}}\left[(\sigma_\rho - \sigma_\phi)^2 + (\sigma_\phi - \sigma_a)^2 + (\sigma_a - \sigma_\rho)^2\right]^{\frac{1}{2}} \tag{7}$$

where σ_ρ, σ_ϕ, and σ_a represent the radial stress, tangential stress, and axial (borehole direction) stress within the rock medium, respectively. The tangential stress $\sigma_\phi = -b\sigma_\rho$, and b is the lateral pressure coefficient, expressed as $b = \mu_\mathrm{d}/(1-\mu_\mathrm{d})$[51].

Moreover, σ_a can be expressed as:

$$\sigma_a = \mu_d(\sigma_\rho + \sigma_\phi) = \mu_d(1-b)\sigma_\rho \tag{8}$$

Therefore, the stress at a specific point within the rock medium in the crushed zone under the influence of an explosion shock wave is given by the following equation:

$$\sigma_i = \frac{1}{\sqrt{2}}\sigma_\rho\left[(1+b)^2 - 2\mu_d(1-b)^2(1-\mu_d) + \left(1+b^2\right)\right]^{\frac{1}{2}} \tag{9}$$

Because the primary difference between uncoupled and coupled charges was the explosive detonation pressure, which resulted in varying initial pressures at the borehole wall, the calculation process for determining the ranges of the crushed and cracked zones remained similar. Therefore, only the coupled charge case was analyzed below.

For coupled charges, the initial compressive stress at the borehole wall caused by the explosive detonation pressure can be expressed as follows[51]:

$$\sigma_i = \frac{2\rho_r C_r}{\rho_r C_r + \rho_e D}\sigma_0 \tag{10}$$

$$\sigma_0 = \frac{1}{1+\gamma}\rho_e D^2 \tag{11}$$

where ρ_r and ρ_e represent the densities of the rock and explosive, respectively (in kg/m^3); C_r and D represent the longitudinal wave velocity of the rock and detonation velocity of the explosive, respectively (in m/s); and γ is the adiabatic coefficient, which can be taken as $\gamma = 3$.

By simultaneously solving Eqs. (6), (9), and (11), the radius of the crushed zone can be obtained as follows:

$$r_{cru} = \left(\frac{\rho_e D^2 AB}{4\sqrt{2}\sigma_{dc}}\right)^{\frac{1}{\alpha}} r_b \tag{12}$$

where $A = \frac{2\rho_r C_r}{\rho_r C_r + \rho_e D}$ and $B = \left[(1+b)^2 + \left(1+b^2\right) - 2\mu_d(1-\mu_d)(1-b)^2\right]^{\frac{1}{2}}$.

Radius of the cracked zone

When the shock wave is attenuated into a stress wave, the stress at a specific point within the cracked zone can be expressed by the following equation:

$$\sigma_{cra}^r = \sigma_j\left(\frac{r_{cru}}{r}\right)^\beta \tag{13}$$

$$\sigma_{cra}^\phi = -b\sigma_{cra}^r \tag{14}$$

where σ_{cra}^ρ and σ_{cra}^ϕ represent the radial and tangential stresses within the cracked zone, respectively. According to Eq. (2), the relationship is given by

$$\sigma_j = \sigma_i\left(\frac{r_b}{r_{cru}}\right)^\alpha \tag{15}$$

By comparing the tangential stress σ_{cra}^ϕ with the dynamic tensile strength σ_{dt}, the radius of the cracked zone can be determined as follows:

$$r_{cra} = \left[\frac{b\sigma_j}{\sigma_{dt}}\right]^{\frac{1}{\beta}} r_{cru} \tag{16}$$

In this experiment, the value of α was not obtained, and the value of r_{cru} could not be determined through calculations. However, the radius of the cracked zone could be estimated based on the measured radius of the crushed zone. According to Eq. (6), the value of σ_{dt} still needs to be determined. The dynamic tensile strength of rock can be influenced by the loading rate[52] and is typically measured using a Hopkinson tensile bar for dynamic direct tensile testing[53] or indirectly determined through the Brazilian disc test using SHPB system[54]. Radial cracks in the blasting cracked zone can result from the dynamic loading Poisson's effect, where the radial

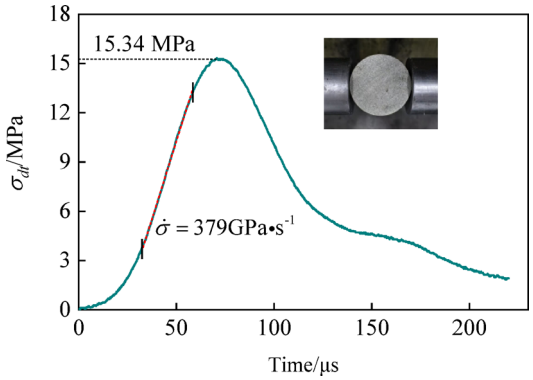

Fig. 15. Dynamic tensile stress-time curve of sandstone.

loading of the blasting stress wave induces lateral tensile failure, which is consistent with the failure mechanism in the Brazilian disc test. A dynamic tensile test was performed on the sandstone specimen adopted in this study under a relatively low impact loading rate using the SHPB system, and the typical stress-time curve is shown in Fig. 15. The dynamic tensile strength of the sandstone specimen was determined to be approximately 15.34 MPa with a stress rate of 379 GPa s^{-1}. Based on the compressive strain rate at the Ω_2 zone boundary and the dynamic elastic modulus, the radial stress rate was calculated to be approximately 4000 GPa s^{-1}, while the tangential stress rate reached about 800 GPa s^{-1}. This suggests that the tangential stress rate at the crack arrest position of radial fractures would exhibit lower magnitudes, potentially approaching the stress rate range obtained from impact tests. Using the obtained stress wave attenuation equation and setting $\mu_d = 0.16$, the radius of the cracked zone was estimated to be approximately 86 r_0, or 0.34 m.

Strict control was applied to the charge and confinement processes in the experiment to achieve ideal columnar charge conditions. The experimental results indicated that the blasting stress waves generated by explosive detonation in the borehole rock mass closely followed cylindrical wave propagation behavior. However, indoor blasting model tests for rocks inherently involve certain challenges in terms of the control and randomness of the results. Owing to the influence of the specimen size and charging method, the errors in the model test analyses can be magnified, thereby serving as a challenge that is difficult to avoid. Regarding the calculated cracked zone range, from the perspective of the r_0-multiple factor, it can be larger than the experimental measurements and findings from other studies, whereas the numerical value of the crack propagation length remained acceptable. In conclusion, the blasting stress wave attenuation law obtained in this study was aligned with practical conditions. Furthermore, although the measured strain or stress values in the Ω_2 region may differ numerically from the actual values, they accurately reflect the attenuation process of the cylindrical stress waves.

Conclusion

An improved constraint device was applied in indoor blasting experiments on columnar rock charges, allowing for testing of the full-field strain evolution process around the borehole rock. This study elucidated the cracking mechanism induced by stress waves, explored the relationship between the dynamic elastic modulus and explosion center distance, derived the stress wave attenuation equation for the cracked zone, and verified the validity of the stress attenuation exponent. The main conclusions are as follows.

(1) The experimental method used in this study satisfied the requirements for columnar charge blasting. The propagation of cylindrical waves represented the process of energy accumulation and release, with the rapid input of blasting energy near the borehole reflected in the downward slope of the strain–time curve. Simultaneously, elastic energy was released radially, promoting the development of circumferential cracks, as indicated by the upward slope. In addition, the rate of energy accumulation exceeded the rate of energy release.
(2) Under columnar charge blasting, the strain rate and dynamic elastic modulus of the rock medium progressively decreased with increasing distance from the explosion center, leading to stress wave attenuation characteristics distinct from those of strain waves. The stress wave attenuation equation followed a power-law form, and the relationship between the stress and strain waves accounted for the strain rate effect on the dynamic elastic modulus of the rock, thereby providing a more accurate representation of the actual conditions.
(3) The complex characteristics of stress-wave attenuation in a rock medium were primarily governed by physical attenuation properties. In both the crushed and cracked zones, the stress wave attenuation was predominantly influenced by physical attenuation. The failure pattern of the specimen, along with theoretical calculations of the cracked zone radius, confirmed the accuracy of the stress wave attenuation equation and validated the experimental method.

Data availability

The datasets used and analysed during the current study are available from the corresponding author on reasonable request.

Received: 7 March 2025; Accepted: 15 May 2025
Published online: 02 July 2025

References

1. Kumar, P., Mohammadi, H., Chopra, R., Tyagi, S. K. & Pandey, S. K. A newly developed blasting cut in tunnels; application of "combined method" in small to medium-sized tunnels. *Tunn. Undergr. Space Technol.* **142**, 105426 (2023).
2. Liu, K. X., Zhang, Y. P., Peng, Y. F. & Wu, L. H. Experimental research and application of drilling and blasting with directional damage-reduction shaped charge. *Sci. Rep.* **14**(1), 1–19 (2024).
3. Li, J. C. Wave propagation across non-linear rock joints based on time-domain recursive method. *Geophys. J. Int.* **193**(2), 970–985 (2013).
4. Zhang, Q. B. & Zhao, J. A review of dynamic experimental techniques and mechanical behaviour of rock materials. *Rock Mech. Rock Eng.* **47**(4), 1411–1478 (2014).
5. Lu, C. P., Dou, L. M., Wu, X. R. & Xie, Y. S. Case study of blast-induced shock wave propagation in coal and rock. *Int. J. Rock Mech. Min. Sci.* **47**(6), 1046–1054 (2010).
6. Chi, L. Y., Zhang, Z. X., Aalberg, A. & Li, C. C. Experimental investigation of blast-induced fractures in rock cylinders. *Rock Mech. Rock Eng.* **52**(8), 2569–2584 (2019).
7. Zhu, F. & Zhao, J. D. Peridynamic modelling of blasting induced rock fractures. *J. Mech. Phys. Solids* **153**, 104469 (2021).
8. Barbosa, N. D. et al. Estimation of fracture compliance from attenuation and velocity analysis of full-waveform sonic log data. *J. Geophys. Res. Solid Earth* **124**(3), 2738–2761 (2019).
9. Walsh, J. B. Seismic wave attenuation in rock due to friction. *J. Geophys. Res.* **71**, 2591–2599 (1966).
10. Far, M. S. & Wang, Y. Probabilistic analysis of crushed zone for rock blasting. *Comput. Geotech.* **80**, 290–300 (2016).
11. Yan, P. et al. Real-Time assessment of blasting damage depth based on the induced vibration during excavation of a high rock slope. *Geotech. Test. J.* **39**(6), 991–1005 (2016).
12. Leng, Z. D., Lu, W. B., Chen, M., Yan, P. & Hu, Y. G. Improved calculation model for the size of crushed zone around blast hole. *Explos. Shock. Waves.* **35**, 101–107 (2015).
13. Chi, L. Y., Zhang, Z. X., Aalberg, A., Yang, J. & Li, C. C. Measurement of shock pressure and shock-wave attenuation near a blast hole in rock. *Int. J. Impact Eng.* **125**, 27–38 (2019).
14. Ding, X. H. et al. The law of blast stress wave propagation and fracture development in soft and hard composite rock. *Sci. Rep.* **12**(1), 1–14 (2022).
15. Jiang, X. D., Xue, Y. G., Ren, X. T., Kong, F. M. & Liao, X. M. Dynamic response characteristics and damage calculation method of fractured rock mass under blasting disturbance. *Int. J. Impact Eng.* **192**, 105036 (2024).
16. Far, M. S., Wang, Y. & Dallo, Y. A. H. Reliability analysis of the induced damage for single-hole rock blasting. *Georisk Assess. Manag. Risk Eng. Syst. Geohazards* **13**(1), 82–98 (2019).
17. Huang, J., Chen, S. H., Liu, M. L. & Li, K. P. Physical model test and numerical simulation study of cumulative damage to deep tunnel surrounding rock under cyclic blasting load. *Int. J. Damage Mech.* **32**(2), 161–184 (2023).
18. Liu, F., Guo, Z. R., Lv, H. Y. & Cheng, Z. B. Test and analysis of blast wave in mortar test block. *Int. J. Rock Mech. Min. Sci.* **108**, 80–85 (2018).
19. Huo, X. F. et al. Attenuation characteristics of blasting stress under decoupled cylindrical charge. *Rock Mech. Rock Eng.* **56**, 4185–4209 (2023).
20. Qiu, J. D. et al. Physical model test on the deformation behavior of an underground tunnel under blasting disturbance. *Rock Mech. Rock Eng.* **54**, 91–108 (2021).
21. Chi, L. Y., Wang, C., Zhang, Z. X., Xu, X. & Yang, J. Experimental investigation of decoupled charge effect on rock fragmentation by blasting. *Rock Mech. Rock Eng.* **55**, 3791–3806 (2022).
22. Wang, S. W., Li, J. C., Li, X. & He, L. Dynamic photoelastic experimental study on the influence of joint surface geometrical property on wave propagation and stress disturbance. *Int. J. Rock Mech. Min. Sci.* **149**, 104985 (2022).
23. Zhu, X. G., Ding, C. X., Sui, Z., Su, H. & Guo, X. Rock fracture mechanism of buffer blasting with cushion layer at the borehole bottom. *Int. J. Miner. Metall. Mater.* **32**(2), 325–334 (2025).
24. Zhang, F. P., Yan, G. L., Peng, J. Y., Qiu, Z. G. & Dai, X. H. Experimental study on crack formation in sandstone during crater blasting under high geological stress. *Bull. Eng. Geol. Environ.* **79**(3), 1323–1332 (2020).
25. Malezhik, M. P., Chernyshenko, I. S. & Sheremet, G. P. Photoelastic simulation of the stress wave field around a tunnel in an anisotropic rock mass subject to shock load. *Int. Appl. Mech.* **42**(8), 948–953 (2006).
26. Yang, R. S., Ding, C. X., Yang, L. Y. & Chen, C. Model experiment on dynamic behavior of jointed rock mass under blasting at high-stress conditions. *Tunn. Undergr. Space Technol.* **74**, 145–152 (2018).
27. Li, X., Zhang, M. & Yang, R. S. Experimental and numerical study on dynamic crack propagation in PMMA under explosive loading using dynamic caustics. *Int. J. Miner. Metall. Mater.* **27**(8), 1256–1268 (2020).
28. He, C. L. & Yang, J. Experimental and numerical investigations of dynamic failure process in rock under blast loading. *Tunn. Undergr. Space Technol.* **83**, 552–564 (2019).
29. Chu, C. Q., Wu, S. C., Zhang, C. J. & Zhang, Y. L. Microscopic damage evolution of anisotropic rocks under indirect tensile conditions: Insights from acoustic emission and digital image correlation techniques. *Int. J. Miner. Metall. Mater.* **30**, 1680–1691 (2023).
30. Liu, H. L., Huang, L. Q., Wang, Z. W., Wu, Y. C. & Li, X. B. Experimental study on dynamic response of hard rock blasting under in-situ stress. *Int. J. Rock Mech. Min. Sci.* **182**, 105860 (2024).
31. Esen, S., Onederra, I. & Bilgin, H. A. Modelling the size of the crushed zone around a blasthole. *Int. J. Rock Mech. Min. Sci.* **40**(4), 485–495 (2003).
32. Chi, L. Y., Wang, C., Zhang, Z. X., Xu, X. & Yang, J. Experimental investigation of decoupled charge effect on rock fragmentation by blasting. *Rock Mech. Rock Eng.* **55**(7), 3791–3806 (2022).
33. Zhu, Q. Q., Li, X. B., Li, D. Y. & Ma, C. D. Experimental investigations of static mechanical properties and failure characteristics of damaged diorite after dynamic triaxial compression. *Int. J. Rock Mech. Min. Sci.* **153**, 105106 (2022).
34. Ye, H. W. et al. Dynamic response characteristics and damage rule of graphite ore rock under different strain rates. *Sci. Rep.* **13**(1), 1–17 (2023).
35. Gao, Z. A., Kong, L. W., Wang, S. J. & Li, T. G. Shear behavior of undisturbed expansive soil under plane strain condition subjected to medium strain rate. *Bull. Eng. Geol. Environ.* **83**(7), 281 (2024).
36. Li, X. B. *Rock Dynamics: Fundamentals and Applications* 119–134 (Science Press, Beijing, 2021).
37. Yin, T. B., Chen, Y. J., Li, X. B. & Li, Q. Effect of high temperature and strain rate on the elastic modulus of rocks: a review. *Int. J. Earth Sci.* **110**(8), 2639–2660 (2021).
38. Li, M., Mao, X. B., Cao, L. L., Mao, R. R. & Pu, H. Experimental study on mechanical properties of coal under high strain rate. *J. Min. Saf. Eng.* **32**(2), 317–324 (2015).
39. Li, M., Mao, X. B., Cao, L. L., Mao, R. R. & Tao, J. Experimental study of mechanical properties on strain rate effect of sandstones after high temperature. *Rock Soil Mech.* **35**(12), 3479–3488 (2014).
40. Shang, J. L., Shen, L. T. & Zhao, J. Attenuation law of stress wave in the Bukit Timah granite. *Chin. J. Rock Mech. Eng.* **20**(2), 212–215 (2001).

41. Yang, R. S. et al. Visualizing the blast-induced stress wave and blasting gas action effects using digital image correlation. *Int. J. Rock Mech. Min. Sci.* **112**, 47–54 (2018).
42. Juneja, A. & Pinaki, P. A numerical study on extent of crushed zone around blasthole in basalt rock. *Geotech. Geol. Eng.* **36**(6), 2577–2588 (2018).
43. Zhang, Z. X. *Rock fracture and blasting: theory and applications* 217–220 (Butterworth-Heinemann, Oxford, 2016).
44. Wang, L. L. *Foundation of stress waves* 252–257 (National Defense Industry Press, Beijing, 2023).
45. Cui, X. Z., Li, W. M., Duan, Z. P. & Chen, S. H. Stress wave attenuation in isotropic damaged rocks. *Explos. Shock. Waves.* **21**(1), 76–80 (2001).
46. Ye, Z. W. et al. Attenuation characteristics of shock waves in drilling and blasting based on viscoelastic wave theory. *Int. J. Rock Mech. Min. Sci.* **171**, 105573 (2023).
47. Nakazawa, S., Watanabe, S., Iijima, Y. & Kato, M. Experimental investigation of shock wave attenuation in basalt. *Icarus* **156**, 539–550 (2002).
48. Zhang, Q. Study on problem of attenuation of explosion stress in rocks by column charges. *Min. Res. Dev.* **10**(3), 63–68 (1990).
49. Khanukaev, A. H. *Physical Process of Ore Rock Blasting*, translated by D. Z. Liu (Metallurgical Industry Press, Beijing, 1980).
50. Wu, F. P. et al. Formation mechanism and main controlling factors of rock's initial damaged zone under explosive impact effect. *Explos. Shock. Waves.* **36**(5), 663–669 (2016).
51. Dai, J. Calculation of rock crushing circle and fracture circle for columnar charge blasting. *J. Liaoning Tech. Univ. Nat. Sci.* **20**(2), 144–147 (2001).
52. Gong, F. Q. & Zhao, G. F. Dynamic indirect tensile strength of sandstone under different loading rates. *Rock Mech. Rock Eng.* **47**(6), 2271–2278 (2014).
53. Han, D. Y., Leung, Y. F. & Zhu, J. B. Tensile strength and deformational behavior of stylolites and mineral healed joints subject to dynamic direct tension. *Rock Mech. Rock Eng.* **55**(6), 1997–2009 (2022).
54. Pei, P. D., Dai, F., Liu, Y. & Wei, M. D. Dynamic tensile behavior of rocks under static pre-tension using the flattened Brazilian disc method. *Int. J. Rock Mech. Min. Sci.* **126**, 104208 (2020).

Acknowledgements

This work was financially supported by Scientific Research Foundation for High-level Talents of Anhui University of Science and Technology(2021yjrc31), the National Natural Science Foundation of China (Nos. 52404071 and 52274071), and the Opening Foundation for the Key Laboratory of Safety Intelligent Mining in Non-coal Open-pit Mines, National Mine Safety Administration(2024-K04).

Author contributions

C.L.: Overall design and guidance. M.W.: Experimental data processing, theoretical analysis and manuscript writing. S.X.: Test instrument operation and assistance. Q.A.: Help with manuscript writing. M.Y.: Help with instrument operation and experimental data processing.

Declarations

Competing interests

The authors declare no competing interests.

Additional information

Correspondence and requests for materials should be addressed to L.C.

Reprints and permissions information is available at www.nature.com/reprints.

Publisher's note Springer Nature remains neutral with regard to jurisdictional claims in published maps and institutional affiliations.